ELSEVIER

Journal of Neuroscience Methods 167 (2008) 367–375

JOURNAL OF NEUROSCIENCE METHODS

www.elsevier.com/locate/jneumeth

Detecting causality between different frequencies

Jianhua Wu [a], Xuguang Liu [b], Jianfeng Feng [a,*]

[a] *Department of Computer Science and Mathematics, University of Warwick, Coventry CV4 7AL, UK*

[b] *Charing Cross Hospital, Division of Neuroscience and Mental Health, Imperial College London, London W6 8RF, UK*

Received 15 May 2007; received in revised form 14 August 2007; accepted 16 August 2007

Abstract

Biological systems are usually non-linear and, as a result, the driving signal frequency (say, M Hz) is in general not identical with the output frequency (say, N Hz). Coherence and causality analysis have been well-developed to measure the (directional) correlation between input and output signals with identical frequencies ($N = M$), but they are not applicable to the cases with different frequencies ($N \neq M$). In this paper, we propose a novel method called *frequency-modified causality* (*coherence*) *analysis* to resolve the issue. The input or output signal is first modulated by up-sampling or down-sampling, coherence and causality analysis are then applied to the frequency modulated and filtered signals. An optimal coherence and causality is found, revealing the true input–output relationship between signals. The method is successfully tested on data generated from a toy model, the van der Pol oscillator and then employed to analyze data recorded from Parkinson's disease (PD) patients.

Keywords: Granger causality; Coherence; Correlation; Parkinson's disease

1. Introduction

Oscillations have been proposed to underlie numerous fundamental computational components of information processing in neural systems (Llinas et al., 1999; Varela et al., 2001). At the cellular level, information carried by action potentials has been analyzed for decades. At the system level, electroencephalogram (EEG) and electromyogram (EMG) have been well studied in physiological and medical fields as well (Llinas et al., 1999; Varela et al., 2001). Although almost all previous researches have concentrated on the correlation or coherence between signals, in recent years, causality analysis between signals has been introduced in dealing with biological data (Albo et al., 2004; Chavez et al., 2003; Ding et al., 2004). One of the most popular methods to calculate causality was proposed by C. Granger (Geweke, 1982; Granger, 1969). It reveals more information than a simple correlation (coherence) analysis: detecting the directional causal influence from one signal to another in the frequency domain. Certainly it can also explore the dynamical causal influence changes along the time and frequency domain (Glass, 1987; Timmer, 2006).

The coherence and causality analysis are well developed in linear cases (Geweke, 1982; Granger, 1969). However, when applying the method to biological data, we often face non-linear systems, and the methods developed in the linear case are not applicable or may even lead to erroneous conclusions. To illustrate the situation, let us define

$$Y(t) = X^{10/3}(t) + X^2(t)\epsilon_t \tag{1.1}$$

and $\epsilon_t \sim N(0, \sigma^2)$ (Fig. 1 left panel is the plot of data). $X(t) = 0.01 * t$, and $t = 1, 2, \ldots, 300$. The correlation between $X(t)$ and $Y(t)$ calculated by the linear assumption is 0.58, but 0.98 by the non-linear assumption. A subsequent and probably more fundamental issue is how to find the true correlation between input and output or, equivalently, the exact form of the input signal. This is certainly a difficult question. To process, we calculate the correlation between $Y(t)$ and $X^{M_0/N_0}(t)$ for $M_0, N_0 = 1, 2, 3, \ldots$ [1] In Fig. 1 right panel, the correlation versus M, N is plotted in a 3D plane. It clearly shows that the correlation attains its maximal values when $M/N = M_0/N_0 = 10/3$ holds. In words, the maximal correlation can reveal the actual input and output relationship.

* Corresponding author. Tel.: +44 2476573788.

[1] We use M_0, N_0 as variables, and M, N as specific value of M_0, N_0.

0165-0270/$ – see front matter © 2007 Elsevier B.V. All rights reserved.
doi:10.1016/j.jneumeth.2007.08.022

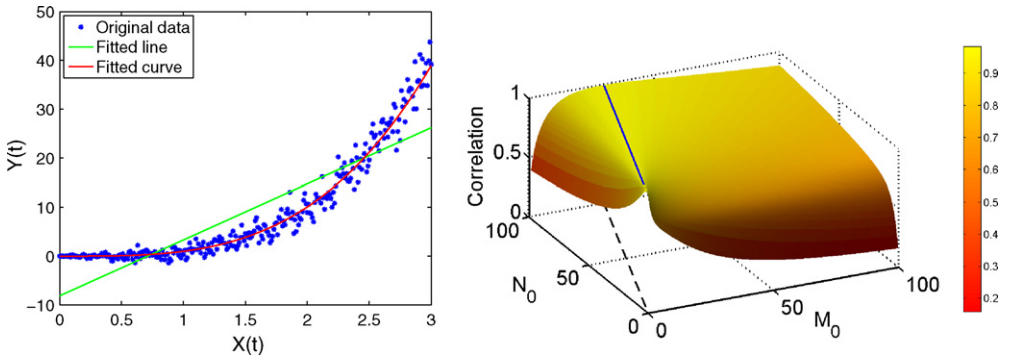

Fig. 1. Left panel is plot of the data: asterisks are the signal pairs, and green line is the linearly fitted line. The red curve is the fitted curve of $Y(t) = X^{10/3}(t)$. Right panel is the correlation plot between $y(t)$ and $X^{M_0/N_0}(t)$ vs. (M_0, N_0). The black line on the M_0, N_0 surface is $M/N = M_0/N_0 = 10/3$. Dashed line is the projection of line $M/N = 10/3$ on the M_0, N_0 plane. (For interpretation of the references to color in this figure legend, the reader is referred to the web version of the article.)

The example above aspires the developments in the current paper. The coherence and causality analysis faces much difficulty when the input–output relationship is non-linear (Chen et al., 2004). As mentioned above, the current research about causality and coherence concentrates on the case of identical input and output frequency cases (linear cases), but the experimental recordings from biology and medicine are not in general linearly correlated. The study of non-linear dynamics in physiology and medicine to explore rhythmic activity has been carried out for years. For example, *M*:*N* phase-locking (Le Van Quyen et al., 2001; Tass et al., 1998) is a typical phenomenon in a non-linear oscillator, where in general $M \neq N$ and M is the input frequency and N is the output frequency. The directionality of the coupling was also studied in many different cases (Bezruchko et al., 2003; Rosenblum and Pikovsky, 2001).

In this paper, we propose a novel method to deal with such types of non-linear signals, usually simultaneously recorded in a biological experiment. By down-sampling and up-sampling either the input or the output signals and filtering, we calculate the coherence or causality between the transformed signals. The optimal coherence or causality is found by scanning over the down-sampling and up-sampling parameters, the similar role played by M_0 and N_0 in Fig. 1.

Our approach is first tested in data generated from a toy model and the van der Pol oscillator. From the obtained coherence or causality, we are able to single out the true input and output signals. The method is then applied to experimental recordings from Parkinson's disease (PD) patients. We know that PD patients have a tremor around 4 Hz in the recorded EMG. There are many papers in the literature where authors try to find the source of the 4 Hz tremor oscillation from the recorded local field potentials (LFP) in subthalamus nucleus (STN), based upon the idea that the driving and output frequency should be identical. In terms of our current approach, we found that the driving frequency in the LFP could be around 8 Hz. Hence an 8:4 phase-locking appears when PD patients start tremor. The existence of a peak at around 8 Hz in the LFP power spectrum has been reported in the literature (Pollok et al., 2004; Timmermann et al., 2003), but it seems our results present the first convincing evidence to assert that 8 Hz could also be the driving frequency in the brain (see also Tass et al., 1998).

2. Methods

The mathematical model of a signal transformation can be described by $Y(t) = f(X(s), s \leq t) + \epsilon_t$, where f is a non-linear transformation function of the driving force $X(t)$ and ϵ_t is the noise. For the model defined above, the simplest case is that the output signal $Y(t)$ is entrained or phase locked to the forcing stimulus $X(t)$. For each M cycles of the stimulus there are N cycles of the output rhythm. The output oscillation occurs at fixed phase (or phases) of the periodic stimulus (*M*:*N* phase-locking). The dependence between these two signals can be approximated as an AR model ($[\tilde{X}(t), \tilde{Y}(t)]$ is the estimate of $[X(t), Y(t)]$)

$$\tilde{X}(t) = \sum_{k=1}^{p} a_{11}(k)\tilde{X}(t-k) + \sum_{k=1}^{p} a_{12}\tilde{Y}(t-k) + u_1(t),$$
$$\tilde{Y}(t) = \sum_{k=1}^{p} a_{21}(k)\tilde{X}(t-k) + \sum_{k=1}^{p} a_{22}\tilde{Y}(t-k) + u_2(t) \qquad (2.1)$$

where the parameter $a_{ij}(k)$ are the model coefficients, $u_1(t)$ is the prediction error when $\tilde{X}(t)$ is predicted from its own past and the past of $\tilde{Y}(t)$, and similarly for $u_2(t)$. The details of the formulation and estimation of AR model is presented in Appendix A. Usually, the optimal model order p can be determined by locating the minimum of the Akaike Information Criterion (AIC) (Lii and Helland, 1981)as a function of the model order p, see Appendix A for more details. The above equations can be expressed in the matrix form as $\xi(t) = [\tilde{X}(t), \tilde{Y}(t)]^{\mathrm{T}}$, $\eta(t) = [u_1(t), u_2(t)]^{\mathrm{T}}$ and $A(k) = -(a_{ij}(k), i, j = 1, 2)$ as following:

$$\xi(t) = -\sum_{k=1}^{p} A(k)\xi(t-k) + \eta(t) \qquad (2.2)$$

Let $A(0) = I$, the identity matrix, Eq. (2.2) can be rewritten as $\sum_{k=0}^{p} A(k)\xi(t-k) = \eta(t)$. The spectral relationship of equation can be written as $A(f)\xi(f) = \eta(f)$, in which $\xi(f) = A^{-1}(f)\eta(f) = H(f)\eta(f)$ and $A(f) = \sum_{k=0}^{p} A(k)\exp(-\mathrm{i}k2\pi f)$. The power spectral matrix of signals is then given by $S(f) = \xi^*(f)\xi(f) = H(f)\eta(f)\eta^*(f)H^*(f) = H(f)\Sigma H^*(f)$ where * stands for conjugate transpose,

$\Sigma = (\Sigma_{ij}, i, j = 1, 2)$ is the covariance matrix of $\eta(t)$, and $S(f) = (S_{ij}(f), i, j = 1, 2)$ is the spectral matrix of $\xi(t)$.

The squared coherence spectrum is given by

$$\gamma^2_{XY}(f) = \frac{|S_{12}(f)|^2}{S_{11}(f)S_{22}(f)} \tag{2.3}$$

According to Geweke's formulation (Geweke, 1982) of Granger causality in the spectral domain, the Granger causality between $X(t)$ to $Y(t)$ is computed according to

$$F_{X\to Y} = \ln \frac{|S_{22}(f)|}{|S_{22}(f) - H_{21}(f)(\Sigma_{11} - \Sigma^2_{12}/\Sigma_{22})H^*_{21}(f)|},$$
$$F_{Y\to X} = \ln \frac{|S_{11}(f)|}{|S_{11}(f) - H_{12}(f)(\Sigma_{22} - \Sigma^2_{21}/\Sigma_{11})H^*_{12}(f)|} \tag{2.4}$$

The measure of causality from $X(t)$ to $Y(t)$ is defined by $F_{X\to Y}$, and symmetrically causality from $Y(t)$ to $X(t)$ is defined by $F_{Y\to X}$. The normalized causality measures are given by

$$R_{X\to Y}(f) = 1 - \exp(-F_{X\to Y}),$$
$$R_{Y\to X}(f) = 1 - \exp(-F_{Y\to X}) \tag{2.5}$$

in the scale of 0–1. Furthermore we denote $\bar{R}_{X\to Y} = \max_f R_{X\to Y}(f)$.

The formulation above is readily applicable to the case of $M = N$. In order to apply Granger causality to the general case of $M \neq N$, the idea is to modify the frequency of one of the signals. For example, if we modify the output frequency by a factor of M/N, the modified output frequency becomes $N \cdot (M/N)$ which is the input frequency, i.e., the input and output signal frequency will be identical and now Granger causality can be applied. To be more precise, denote $Y[n] = Y(nT_s)$ where $1/T_s$ is the sampling rate of $Y(t)$ and $n = 1, 2, 3, \ldots$. For an integer M_0, we define $Y^{(M_0)}[n] = Y[nM_0]$, down-sampling $Y[n]$ by a factor M_0; and then up-sampling $Y^{(M_0)}[n]$ with a factor N_0, i.e., $Y^{(M_0/N_0)}[n] = Y^{(M_0)}[\text{int}(n/N_0)]$, where $\text{int}(x)$ is the integer part of x. In general, it is easily seen that down-sampling and up-sampling will introduce aliasing and image frequencies. To avoid aliasing, a lowpass filter is usually applied after down-sampling and up-sampling (see for example, Chapter 6 in Cristi, 2004 for details). The relationship between the z-transform of $Y(t)$ and $Y^{(M_0/N_0)}(t)$ is similar to the relationship in Eq. (1.1).

After performing the down-sampling, up-sampling (frequency-modification) and filtering, and denoting the obtained signal as $Z(t) = Y^{(M_0/N_0)}(t)$ or $Z(t) = X^{(N_0/M_0)}(t)$, the coherence and causality analysis can be directly applied to $X(t)$ or $Y(t)$ and $Z(t)$. In real applications, the length of two sequences are then not identical, say, $\text{length}(X(t)) > \text{length}(Z(t))$. We simply truncate the sequence $X(t)$ to the length of $Z(t)$. The maximal value of the causality and coherence will tell us the actual driving frequency of the input signal and output signal. We call the approach presented here *frequency-modified causality (coherence) analysis* (FM causality (coherence)).

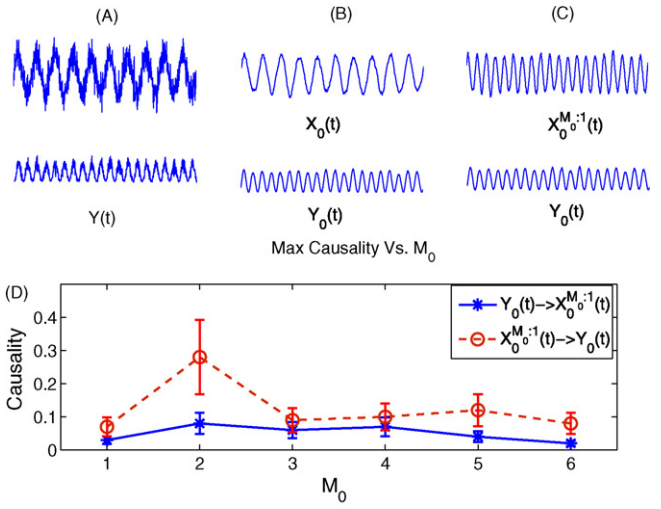

Fig. 2. Panel (A) is the plot for input $X(t)$ and output signals $Y(t)$ with noise. Panel (B) is the plot for input $X_0(t)$ and output signals $Y_0(t)$ with noise filtered by low bandpass filter. Panel (C) shows plot for filtered signals. The input signal $X(t)$ is down-sampled such that the transformed signal $X_0^{(2/1)}(t)$ has the same frequency as $Y_0(t)$. Panel (D) shows the maximum causality between transformed signal $X_0^{(2/1)}(t)$ and output signal $Y_0(t)$. When M: $N = M_0$: $N_0 = 2$, the causality from $X_0^{(2/1)}(t)$ to $Y_0(t)$ reaches its maximum.

3. Applications: synthesized data

To verify our approach, we first apply it to two artificial datasets.

3.1. Toy model

Define $X(t) = \sin(\omega t) + \epsilon_t$, $Y(t) = 1/2 - 1/2\cos(2\omega(t-1)) + \sin(\omega t)\epsilon_t = \sin^2(\omega(t-1)) + \sin(\omega t)\epsilon_t$, where $\omega = 20\pi$, and ϵ is normally distributed noise. The signals are sampled at 1000 Hz, as plotted in Fig. 2(A). Obviously, the input $X(t)$ is the causal of the output $Y(t)$. Before applying the causality analysis, the signals are first filtered by a low bandpass filter. The filtered signals $(X_0(t), Y_0(t))$ are plotted in Fig. 2(B). It is obvious that the frequency of the input signal is two times larger than that of the output signal, i.e., the input and output are in the regions of (M: $N = 2$:1). Then the input filtered signal is down-sampled such that the transformed signal $X_0^{(N/M)}(t)$ has the same frequency as $Y(t)$, see Fig. 2(C). The obtained causality results are shown in Fig. 2(D). Comparing the blue lines (causality from $X_0^{(M_0/1)}(t)$ to $Y_0(t)$) with the red lines (causality from $Y_0(t)$ to $X_0^{(M_0/1)}(t)$), it is clearly seen that both causalities increase considerably for FM data. The causality reaches its maximum when M: $N = M_0$: $N_0 = 2$:1, which is exactly the phase-locking between the output and input signals.

3.2. van der Pol oscillator

The periodically forced van der Pol equation can be written as $d^2Y(t)/dt^2 - \psi(1 - Y^2(t))(dY(t)/dt) + Y(t) = BX(t)$ where $X(t)$ could be a sinusoid $\cos(\nu t)$ or $\sin(\nu t)$. When $B = 0$, there is a unique stable limit cycle oscillation. When $X(t) =$

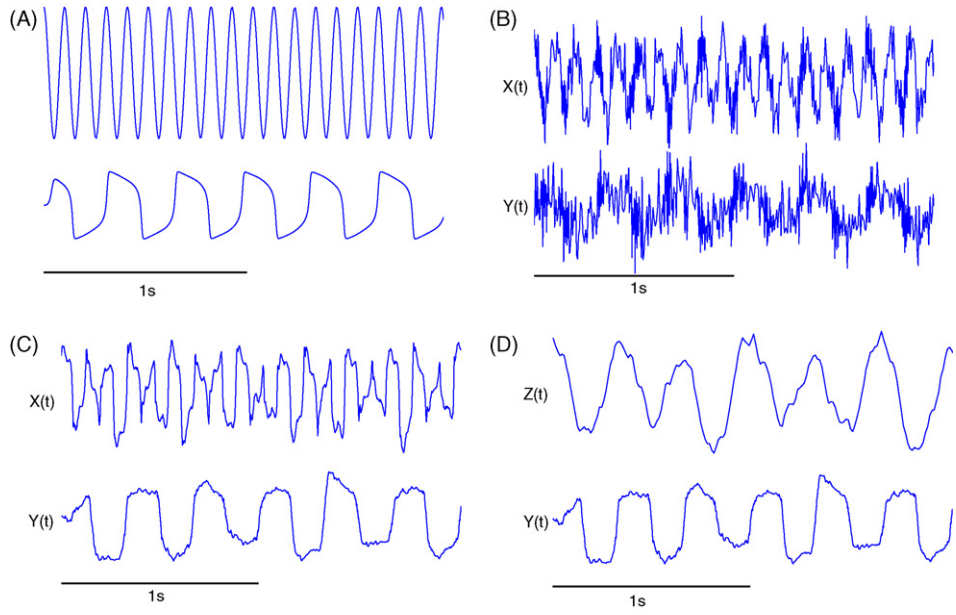

Fig. 3. Panel (A) is the plot for input $X(t)$ and output signals $Y(t)$ without noise. Panel (B) is the plot for input $X(t)$ and output signals $Y(t)$ with noise added to $X(t)$. Panel (C) shows plot for filtered signals. The input signal $X(t)$ is up-sampled such that the transformed signal $Z(t)$ has the same frequency as $Y(t)$. Signals $Z(t)$ and $Y(t)$ are plotted in panel (D).

$\cos(\nu t)$, as ν and B vary, there are entrainment regions, which have been extensively studied in the literature.

The input signal is $X(t) = \cos(\nu t) + \epsilon_t$, where the noise term $\epsilon_t \sim N(0, \sigma^2)$. The input signal is sampled at 1000 Hz, and the total sample length is 10^4. Due to different parameters in the oscillator, the output signal is phase locked by various periods M_0: N_0. In the current setup, we use $\psi = 4$, $\nu = 18\pi$, $B = 20$, and $\sigma^2 = 0.2$. Before applying the causality and coherence analysis, the signals are first filtered by a lowpass filter. The original and filtered signals are presented in Fig. 3. It is obvious that the frequency of the input signal is three times of that of the output signal, i.e., the input and output is in the regions of (M: $N = 3$:1) phase-locking.

To make the problem more realistic, a sinusoid signal $W(t)$, with the same frequency to the input signal $X(t)$, is added to the output signal $Y(t)$, i.e., $Y_0(t) = W(t) + Y(t) + \epsilon_t$. The intensity of the power spectrum of $W(t)$ is equal to that of $X(t)$. If the causality analysis is directly applied to the filtered signals, there is directional causality at two specific frequencies at 3 and 9 Hz (see the blue solid line in Fig. 4(E)). But the causality at the frequency 9 Hz is even more stronger than that at frequency 3 Hz. The same conclusion is true for coherence analysis (see the blue solid line in Fig. 4(D)). One might wrongly conclude that there is an input signal at 9 Hz which generates an output signal at 9 Hz. Of course we know the causality and coherence peak at 9 Hz is simply due to the added 'noise' signal $W(t)$. The results tell us that a direct application of the causality or coherence analysis could be very misleading.

Now we carry out FM causality and coherence analysis. The input signal $X(t)$ is first up-sampled such that the transformed signal $X^{(N_0/M_0)}(t)$ has the same frequency as $Y(t)$, as shown in Fig. 3. The obtained causality and coherence results are shown in Fig. 4(D) and (E) (red solid and dotted lines). Comparing the blue lines (causality and coherence between $X(t)$ and $Y_0(t)$) with red lines (causality and coherence between $X^{(N_0/M_0)}(t)$ and $Y_0(t)$), it is clearly seen that both coherence and causality increase considerably for modified data.

Next we intend to demonstrate that the causality and coherence between $X^{(N_0/M_0)}(t)$ and $Y_0(t)$ attain their maximal value with respect to all possible M_0, N_0. In Fig. 4(F), the causality between $X^{(N_0/M_0)}(t)$ and $Y_0(t)$ with respect to M_0, N_0 is depicted, where $M_0 \in \{1, 2, 3, \ldots, 10\}$, $N_0 = 1$. The purple circles are the causality from $Y_0(t)$ to $X^{(N_0/M_0)}(t)$, and the red stars are the causality from $X^{(N_0/M_0)}(t)$ to $Y_0(t)$. When $M = M_0 = 3$, the causality from $X^{(N_0/M_0)}(t)$ to $Y_0(t)$ reaches its global maximum, clearly indicating that the actual output signal $Y_0(t)$ at 3 Hz is driven by an input signal at 9 Hz.

The obtained results shown in Fig. 4 are convincing and clearly indicate the power of our approach. The added 'noise' signal has a power spectrum as strong as the original output signal, i.e., the signal to noise ratio (SNR) is unity, but our approach is still capable of picking out the true input and output signal. We have carried out a systematic investigation on the impact of SNR on the outcome of our approach (see Section 5).

4. Application: Parkinson's disease

Local field potentials (LFPs) from subthalamic nucleus (STN) and surface electromyograms (EMGs) simultaneously recorded from the contralateral forearm muscles were collected, with the hope of revealing some intrinsic properties between brain activities and the forearm movement and to achieve a better treatment of PD (deep-brain-stimulation) (Liu et al., 2002; Wang et al., 2005). The study was approved by the local research ethics committee, detailed surgical procedures and target localization have been described in the literature (Liu et al., 2002).

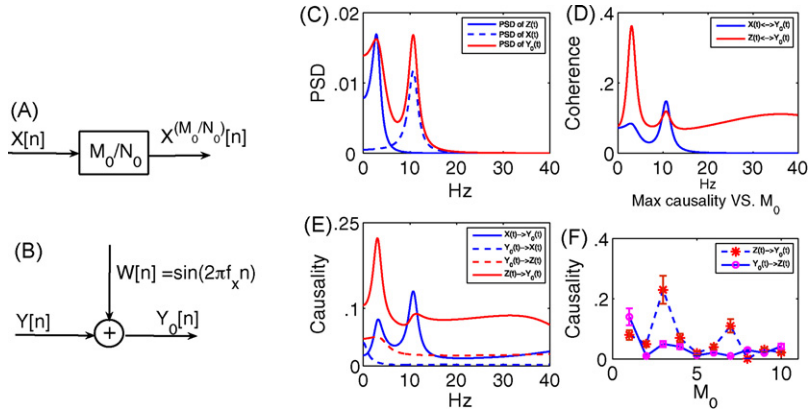

Fig. 4. (A) and (B) Schematic plot of data acquisition. (C) Power spectrum of $X(t)$, $Y_0(t)$ and $Z(t)$. (D) The coherence plots. (E) Directional causality between $X(t)$ and $Y_0(t)$ (blue curves), and causality between $Z(t)$ and $Y_0(t)$ (red curves). (F) Plots $\bar{R}_{X^{(N_0/M_0)}(t)\to Y_0(t)}$ and $\bar{R}_{Y_0(t)\to X^{(N_0/M_0)}(t)}$ vs. $M_0 = 1, 2, \ldots, 10$, $N_0 = 1$. The confidence interval for maximum causality is constructed by using bootstrap method. The confidence interval clearly indicates that the causality reaches its maximum when $N : M = 1{:}3$. (For interpretation of the references to color in this figure legend, the reader is referred to the web version of the article.)

LFPs were recorded with a bipolar configuration from the adjacent four contacts of each macro-electrode (0–1, 1–2, 2–3) with a common electrode placed on the surface of the mastoid. EMGs were recorded using surface electrodes placed in a tripolar configuration over the tremulous forearm extensor and flexors. Only one channel of EMGs is used in our analysis. The detailed experiment and data acquisition could be referred to (Liu et al., 2002; Wang et al., 2005, 2006). It is believed that the forearm tremor is driven by the neuronal activities in STN (Brovelli et al., 2004; Lii and Helland, 1981; Pollok et al., 2004; Timmermann et al., 2003). Coherence and causality analysis have been employed to analyze the time-dependent causal influence between the LFPs and EMGs (Brovelli et al., 2004; Timmermann et al., 2003), but the analysis is simply based on the assumption that the driving frequency of LFPs is identical to that of EMGs. The obtained results showed that there is a directional causality predominantly

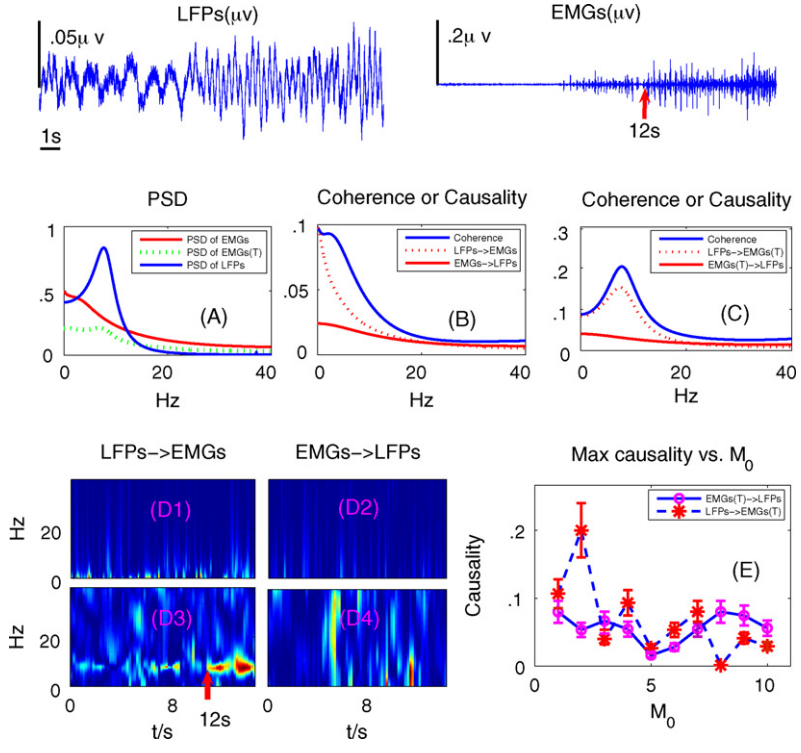

Fig. 5. Panel (A) shows power spectrum density (PSD) of the signals $X(t)$ (LFP), $Y(t)$ (EMG) and $Y^{(2/1)}(t)$. Panels (B) and (C) are the coherence and causality plots for $X(t)$, $Y(t)$ and $X(t)$, $Y^{(2/1)}(t)$, respectively. The blue cure is the coherence between LFPs and EMGs. The red dotted curve is the directional causality from LFPs to EMGs, and the red curve is the directional causality form EMGs to LFPs. EMGs(T) stands for the transformed EMGs signal. D1 ($X(t) \to Y(t)$), D2 ($Y(t) \to X(t)$) and D3 ($X(t) \to Y^{(2/1)}(t)$), D4 ($Y^{(2/1)}(t) \to X(t)$) are the time-dependent causality spectrum plots between LFPs and EMGs. E plots $\bar{R}_{X(t)\to Y^{(M_0/N_0)}(t)}$ and $\bar{R}_{Y^{(M_0/N_0)}(t)\to X(t)}$ vs. $M_0 = 1, 2, \ldots, 10$, $N_0 = 1$. The confidence interval for maximum causality is constructed by using bootstrap method. (For interpretation of the references to color in this figure legend, the reader is referred to the web version of the article.)

from LFPs to EMGs, at the forearm tremor frequency of around 4 Hz. Some authors have also observed that there is a peak in the power spectrum at around 8 Hz in STN (Brovelli et al., 2004; Pollok et al., 2004; Timmermann et al., 2003), and that the 4 Hz tremor is driven by the 8 Hz signal. There is no direct evidence whether 8 Hz drives 4 Hz or 4 Hz drives 4 Hz and is a currently hotly debating issue. Our developments presented herein provide us with possible tools to resolve the debate.

The original LFPs ($X(t)$) and EMGs ($Y(t)$), both sampling frequency are 500 Hz, can be found at our website (http://www.dcs.warwick.ac.uk/~feng/fm). The tremor frequency of forearm is predictable (4 Hz), and can be described by recorded EMGs. The EMGs are down-sampled with a parameter M_0, where M_0 varies from 1 to 10, i.e., $Z(t) = Y^{(M_0/N_0)}(t)$. A detailed comparison between $(X(t), Y(t))$ and $(X(t), Y^{(2/1)}(t))$ for power spectrum density, causality, coherence and time-frequency causality is presented in Fig. 5 for one patient. The power spectrum density for original and modified EMGs data does not have any significant changes (Fig. 5(A)), but the coherence and causality between LFPs and EMGs have significant changes after frequency-modification (Fig. 5(B, C and D). The coherence and directional causality reach their maximum at the frequency 9.1 Hz (Fig. 5(E)). In Fig. 5(C), dotted red line clearly shows that there is a strong causal influence from LFPs to EMGs at the frequency 9.1 Hz, but the feedback from EMGs to LFPs is much weak. The time-dependent spectrum (Fig. 5(D)), reveals more details about the causal influence from LFPs to EMGs. It shows that at around 12 s, the influence from LFPs to EMGs becomes strong and persistent (commencing of tremor). This phenomenon is also in consistent with the behavior data, where the forearm tremor starts at around 12 s (see http://www.dcs.warwick.ac.uk/~feng/fm). This is certainly a clear validation of our results. Finally, in Fig. 5(E) we plot the causality between STN and arm activity with respect to $M_0 = 1, 2, \ldots, 10$, $N_0 = 1$. From the figure, it is shown that there is no clear directional causality for any frequency for $M_0 = 1$ and M_0 being equal to or greater than 3, $N_0 = 1$. The maximum causality is attained at $M = 2$, $N = 1$. Our results tell us that the tremor for the PD patient is driven by STN activities, but with a phase-locking of 8:4 rather than 4:4 as reported in the literature.

Table 1
Phase-locking (P.L.) vs. the maximum causality for seven patients (Pa.)

P.L.	Pa.						
	1	2	3	4	5	6	7
1:1	.31[a]	.28[a]	.11	.06	.29[a]	.24[a]	.10
1:2	.12	.09	.32	.25[b]	.14	.09	.21[b]
1:3	.08	.04	.08	.05	.10	.06	.07
1:4	.03	.07	.06	.10	.08	.02	.03

[a] The patient with a 4:4 phase-locking.
[b] The patient with a 8:4 phase-locking.

The maximum causality (see Fig. 5) vs. different phase-lockings is summarized in Table 1 for a total of seven patients. We have tested all seven PD patients and found that four out of seven have a phase-locking of 4:4, three out of seven a phase-locking of 8:4. The details of maximum causality against M_0: N_0 are illustrated in Fig. 6. The physiological meaning of our finding is currently under clinical testing.

5. Discussion

We have only shown three examples of applications, however, there are increasing number of cases in biology where our methods can be applied. Although there is still both computational and mathematical development, by extending the concepts derived here, it is clear that our approach could allow automated construction of network structures, not only between two but also across multiple simultaneously recorded signals in an increasing number of biological contexts (Feng et al., 2006; Sachs et al., 2005). The method would be extremely useful when the signals are stationary, because the parameters estimation from AR model is much more accurate. When the signals are non-stationary, it is also applicable by using sliding windowed AR model.

5.1. Bicoherence and phase synchronization index

In the literature (Collis et al., 1998; Jamšek et al., 2004), bispectrum and bicoherence analysis have been proved to be useful for analyzing systems with asymmetric non-linearities. It

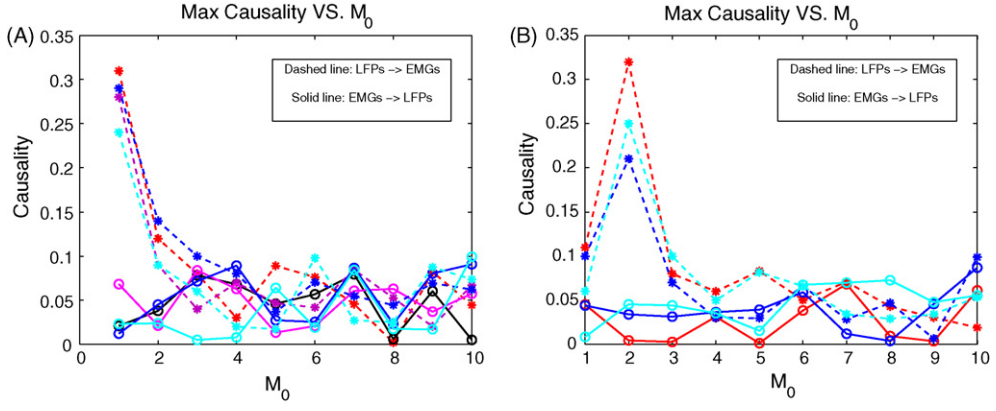

Fig. 6. Panel (A) and (B) shows the maximum causality plot against different values of M ranging from 1 to 10. In panel (A), the results show 1:1 phase-locking exists between LFPs and EMGs for all four patients. In panel (B), the results show 2:1 phase-locking exists between LFPs and EMGs for all three patients.

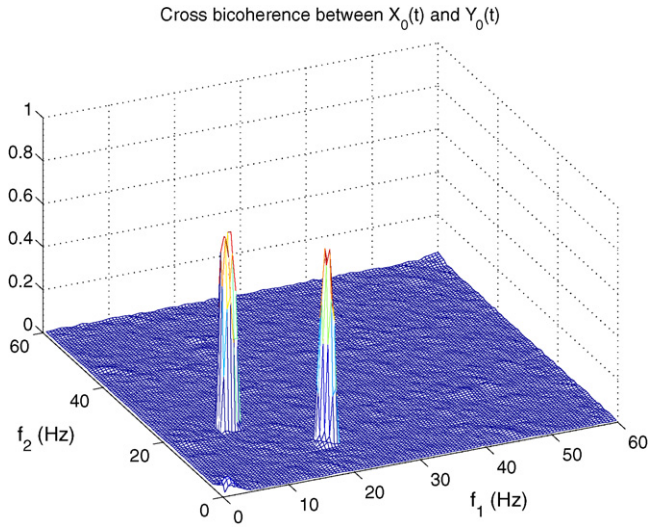

Fig. 7. Cross bicoherence plot between input and output signals across the frequency.

can detect non-Gaussianity of the signal or the non-linear interactions between two signals. To compare our approach (FM causality or coherence analysis), we employed cross bicoherence analysis to study the frequency relationship between two signals in our toy model. Fig. 7 demonstrates the bicoherence between input and output signals across the frequency domains. It is obvious that bicoherence can also detect the phase-locking relationship between the two signals. We have also compared our approach with another well-known phase-locking detection method (phase synchronization index (PSI)) proposed by Tass (Tass et al., 1998). The results presented by both approaches are consistent.

Nevertheless, our approach tells us not only the phase-locking information (coherence), but also the directional information (causality). It is also possible that the bicoherence analysis can be further extended to causality analysis, but such an extension has not be reported in the literature yet. Furthermore, other statistical quantities such as confidence intervals and partial coherence and causality (Guo and Feng, in preparation) could be easily adopted to FM causality analysis.

5.2. Signal to noise ratio

One may suggest that the observed phenomena in Parkinson's data is due to an artefact causing by noise: the 8 Hz is a harmonic frequency of 4 Hz and noise could shift everything from 4 to 8 Hz. The effect of noise may obscure the true coherence and causality analysis (Timmermann et al., 2003) by altering their values. Here we develop a simple test to demonstrate that only when the noise to signal ratio exceeds a certain unrealistic level, it could result in an artefact. Two sinusoid signals with identical frequency of 5 Hz are added with white noise with a noise to signal ratio r. We concluded that when the noise to signal ratio r is less than 3, the peak of PSD, cross-spectrum and coherence are always at the true frequency, rather than at its harmonics. Fig. 8 demonstrates the results when r is 2. It shows that all

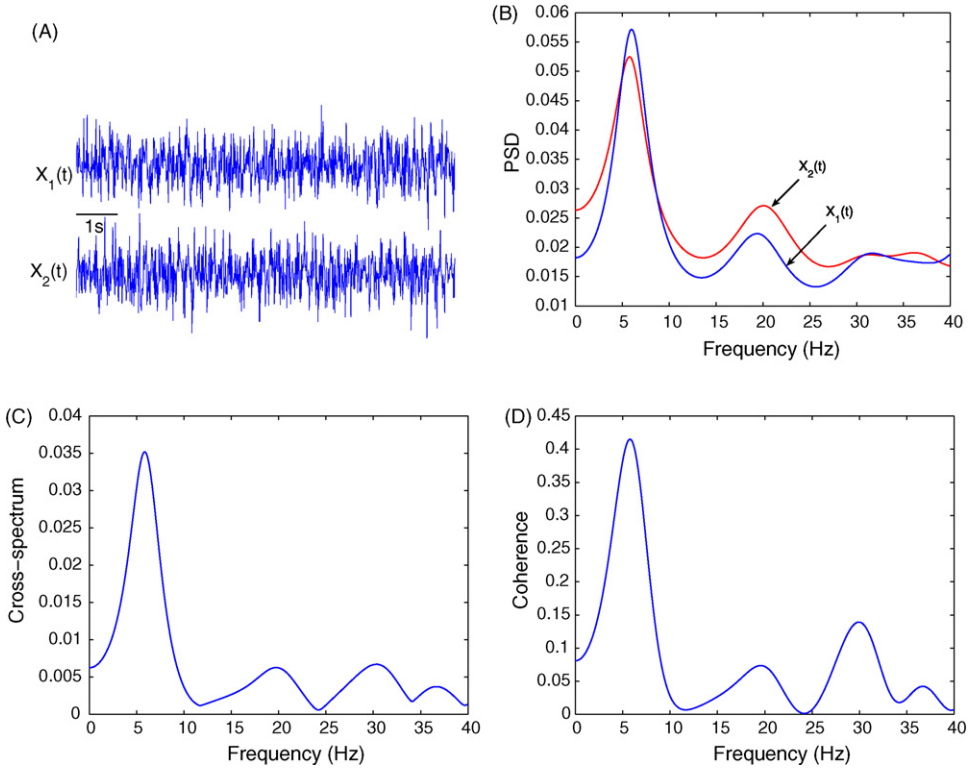

Fig. 8. Panel (A) shows the sinusoid signals with added white noise. The noise-signal ratio r is 2. Panel (B) is the power spectrum of the signals. Harmonic components occurs at 20 Hz. Panel (C) shows the cross-spectrum between two signals. Panel (D) is the coherence between two signals. Both cross-spectrum and coherence show that the true correlation between two signals.

quantities at the harmonic frequencies are much less than they are at the actual frequency.

5.3. True drive frequency

In our approach, we have formulated an analytical approach to reveal the actual drive frequencies between two channels. The idea is to fix one channel, but down- or up-sampling the other channel so that we could apply the analytical method of linear case to the data. After scanning over all frequencies, we regard the frequencies corresponding to the maximum causality or coherence as the true drive frequencies. We have tested our approach in two cases and they both work very well. However, we want to emphasize here that our approach, more or less a heuristic one, is based upon our belief that the maximal value should correspond to the true drive frequency. We are certainly unable to provide an analytical proof. The final confirmation of the obtained results should only come from a direct experiment, but our approach definitely could provide us with valuable information.

Appendix A. Model fitting

Let $A(0) = I$, the identity matrix, Eq. (2.2) can be rewritten as

$$\sum_{k=0}^{p} A(k)\xi(t-k) = \eta(t) \tag{A.1}$$

where $A(i)$ $(i = 0, 1, 2, \ldots, p)$ are 2×2 coefficient matrices and $\eta(t) = [u_1(t), u_2(t)]^{\mathrm{T}}$ is a zero mean uncorrelated process with covariance matrix Σ.

To estimate $A(i)$ and Σ, we multiply Eq. (A.1) by $\xi^{\mathrm{T}}(t-k)$, where $k = 1, 2, \ldots, p$. Taking expectation, we obtain the Yule-Walker equations

$$\sum_{i=0}^{p} A(i)R(-k+i) = 0 \tag{A.2}$$

where $R(n) = \langle \xi(t)\xi^{\mathrm{T}}(t+n)\rangle$ is $\xi(t)$'s covariance matrix of lag n. Here we note that $R^{\mathrm{T}}(n) = R(-n)$. In deriving these equations, we have used the fact that $\langle \eta(t)\xi^{\mathrm{T}}(t-k)\rangle = 0$ as a result of $\eta(t)$ being an uncorrelated process.

For a single realization of the ξ process, $\{\xi(i)\}_{i=1}^{N}$ (N is data length for a single trial), we compute the covariance matrix in Eq. (A.2) according to

$$\tilde{R}(n) = \frac{1}{N-n}\sum_{i=1}^{N-n} \xi(i)\xi^{\mathrm{T}}(i+n) \tag{A.3}$$

If multiple realizations of the same process are available, then we compute the above quantity for each realization and average across all the realizations to obtain the final estimate of the covariance matrix. Note that for a single short trial of data one uses the divisor N for evaluating covariance to reduce inconsistency. Due to the availability of multiple trials we have used the divisor $(N-n)$ in the above definition Eq. (A.3) to achieve an unbiased estimate. It is quite clear that, for a single realization, if N is small, one will not get good estimates of $R(n)$ and hence will not be able to obtain a good model. This problem can be overcome if a large number of realizations of the same process are available. In this case the data length can be as short as the model order p plus 1.

Eq. (A.1) contains a total of $4p$ unknown model coefficients. In Eq. (A.2) there are exactly the same number of linear equations. One can simply solve these equations to obtain the model coefficients. The Levinson, Wiggins and Robinson (LWR) algorithm (Haykin and Kesler, 1983; Morf et al., 1978) is a more robust solution procedure, based on the ideas of maximum entropy. This algorithm can be implemented in solving Eq. (A.3). The noise covariance matrix Σ can be obtained as part of the LWR algorithm. Otherwise one may obtain Σ through

$$\Sigma = R(0) + \sum_{i=1}^{p} A(i)R(i) \tag{A.4}$$

The above estimation procedure can be carried out for any model order p. The model order p is usually determined by minimizing the Akaike Information Criterion (AIC) (Akaike, 1974; Lii and Helland, 1981) defined as

$$\mathrm{AIC}(p) = \frac{2\,\log[\det(\Sigma)] + 8p}{N_{\mathrm{total}}} \tag{A.5}$$

where N_{total} is the total number of data points from all the trials, $\det(\Sigma)$ is the determinant of Σ.

References

Albo Z, Di Prisco GV, Chen YH, Rangarajan G, Truccolo W, Feng JF, et al. Is partial coherence a viable technique for identifying generators of neural oscillations. Biol Cybern 2004;90:318–26.

Akaike H. A new look at the statistical model identification. IEEE Trans Automat Contr 1974;19:716–23.

Bezruchko B, Ponomarenko V, Rosenblum MG, Pikovsky AS. Characterizing direction of coupling from experimental observations. Chaos 2003;13:179–84.

Brovelli A, Ding MZ, Ledberg A, Chen YH, Nakamura R, Bressler SL. Beta oscillations in a large-scale sensorimotor cortical network: directional influences revealed by Granger causality. PNAS 2004;101:9849–54.

Chavez M, Martinerie J, Le Van Quyen M. Statistical assessment of nonlinear causality: application to epileptic EEG signals. J Neurosci Meth 2003;124:113–28.

Chen YH, Rangarajan G, Feng JF, Ding MZ. Analyzing multiple non-linear time series with extended Granger causality. Phys Lett A 2004;324:26–35.

Collis W, White PR, Hammond JK. Higher-order spectra: the bispectrum and trispectrum. Mech Syst Signal Process 1998;14:375–94.

Cristi R. Modern digital signal processing. New York: Brooks, Cole; 2004.

Ding MZ, Bressler SL, Yang WM, Liang HL. Short-window spectral analysis of cortical event-related potentials by adaptive multivariate autoregressive modeling: data preprocessing, model validation, and variability assessment. Biol Cybern 2004;83:35–45.

Feng JF, Jost J, Qian MP. Network: from biology to theory. London: Springer-Verlag; 2006.

Guo SX, Feng JF. Partial Granger causality, eliminating exogenous inputs and latent variables, in preparation.

Geweke J. Measurement of linear dependence and feedback between multiple time series. J Am Stat Assoc 1982;77:304–24.

Glass L. From clocks to chaos: the rhythms of life. Princeton University Press; 1987.

Granger C. Investigating causal relations by econometric models and cross-spectral methods. Econometrica 1969;37:428–38.

Haykin S, Kesler S. Nonlinear methods of spectral analysis. Berlin Heidelberg New York: Springer; 1983.

Jamšek J, Stefanovska A, McClintock P. Nonlinear cardio-respiratory interactions revealed by time-phase bispectral analysis. Phys Med Biol 2004;49:4407–25.

Le Van Quyen M, Foucher J, Lachaux J, Rodriguez E, Lutz A, Martinerie J, et al. Comparison of Hilbert transform and wavelet methods for the analysis of neuronal synchrony. J Neurosci Meth 2001;111:83–98.

Lii L, Helland K. Cross-Bispectrum Computation and Variance Estimation. ACM Trans Math Software 1981;7:284–94.

Llinas RR, Ribary U, Jeanmonod D, Kronberg E, Mitra P. Thalamocortical dysrhythmia: a neurological and neuropsychiatric syndrome characterized by magnetoencephalography. PNAS 1999;96:15222–7.

Liu X, Nandi D, Winter JL. Deep brain stimulation of the pedunculopontine region in the normal non-human primate. Clin Neurophysiol 2002;113:1667–72.

Morf M, Vieira A, Lee DTL, Kailath T. Recursive multichannel maximum entropy spectral estimation. IEEE Trans Geosci Electron 1978;16: 85–94.

Pollok B, Gross J, Dirks M, Timmermann L, Schnitzler A. The cerebral oscillatory network of voluntary tremor. J Neurophysiol 2004;554:871–8.

Rosenblum MG, Pikovsky AS. Phase synchronization of chaotic oscillators. Phys Rev E 2001;64:45202.

Sachs K, Perez O, Pe'er D, Lauffenburger DA, Nolan GP. Causal protein-signaling networks derived from multiparameter single-cell data. Science 2005;308:523–9.

Tass P, Rosenblum MG, Weule J, Kurths J, Pikovsky A, Volkmann J, et al. Detection of n:m phase-locking from noisy data: application to magnetoencephalography. Phys Rev Lett 1998;81:3291–4.

Timmer J. Handbook on time series analysis. Wiley; 2006.

Timmermann L, Gross J, Dirks M, Volkmann J, Freund HJ, Schnitzler A. The cerebral oscillatory network of Parkinsonian resting tremor. Brain 2003;126:199–212.

Varela F, Lachaux JP, Rodriguez E, Martinerie J. The brainweb: phase synchronization and large-scale integration. Nat Rev Neurosci 2001;2:229–39.

Wang SY, Chen YH, Ding MZ, Feng JF, Stein JF, Aziz TZ, et al. Revealing the dynamic correlation between neural and muscular signals using time-dependent Granger causality analysis. Proc IEE Med Appl Signal Process 2005;2:99–105.

Wang SY, Aziz TZ, Stein JF, Bain PG, Liu XG. The physiological and harmonic components in neural and muscular coherence in Parkinsonian tremor. Clin Neurophysiol 2006;117:1487–98.